Influence of temperature, doping, and amorphization on the electronic structure and magnetic damping of iron

Zhihao Jiang [1], Axel Hoffmann,[1,2] and André Schleife [1,2,3,*]

[1]*Department of Materials Science and Engineering, University of Illinois, Urbana-Champaign, Urbana, Illinois 61801, USA*
[2]*Materials Research Laboratory, University of Illinois at Urbana-Champaign, Urbana, Illinois 61801, USA*
[3]*National Center for Supercomputing Applications, University of Illinois at Urbana-Champaign, Urbana, Illinois 61801, USA*

Hybrid magnonic quantum systems have drawn increased attention in recent years for coherent quantum information processing, but too large magnetic damping is a persistent concern when metallic magnets are used. Their intrinsic damping is largely determined by electron-magnon scattering induced by spin-orbit interactions. In the low-scattering limit, damping is dominated by intraband electronic transitions, which has been theoretically shown to be proportional to the electronic density of states at the Fermi level. In this work, we focus on body-centered-cubic iron as a paradigmatic ferromagnetic material. We comprehensively study its electronic structure using first-principles density functional theory simulations and account for finite lattice temperature, boron (B) doping, and structure amorphization. Our results indicate that temperature-induced atomic disorder and amorphous atomic geometries only have a minor influence. Instead, boron doping noticeably decreases the density of states near the Fermi level with an optimal doping level of 6.25%. In addition, we show that this reduction varies significantly for different atomic geometries and report that the highest reduction correlates with a large magnetization of the material. This may suggest materials growth under external magnetic fields as a route to explore in experiment.

I. INTRODUCTION

Hybrid magnonics is gaining growing interest due to its potential for coherent quantum information processing [1–4]. This was triggered by the experimental demonstration of coherent coupling between a magnon and a superconducting qubit, mediated by a microwave cavity, by Tabuchi *et al.* [5] As one key ingredient in hybrid magnonic systems, magnons possess unique advantages such as easily tunable resonance frequencies through external magnetic fields or materials anisotropy, microwave bandwidths that match state-of-the-art superconducting quantum devices, and intrinsic nonreciprocity that is promising for noise-resilient quantum state transduction [4,6]. In recent years, more research has established coupling between magnons and microwave photons in a cavity or a coplanar circuit structure [7–10].

However, one essential challenge is the damping of magnon excitations that limits the coherence time of hybrid quantum states [4,11]. Therefore, exploring materials with low magnetic damping is crucial for achieving hybrid magnonic quantum devices with long coherence time. One of the best-known materials in this context is the ferrimagnetic insulator yttrium iron garnet (YIG), $Y_3Fe_5O_{12}$, whose magnetic damping parameter can be as low as 10^{-5} in bulk crystals [12]. However, insulators such as YIG are not desired for many spintronics applications that require a charge current through the material [13]. In addition, YIG is not well suited to

be integrated into on-chip devices for circuit quantum electrodynamics due to experimental constraints. One of the reasons is that, in order to have sufficient crystalline quality for low damping, YIG films need to be grown on specific substrates to achieve epitaxy. The standard substrate choice for this task is gadolinium gallium garnet, $Gd_3Ga_5O_{12}$, but at very low temperatures the increased magnetic susceptibility due to ordering of the Gd magnetic moments can increase the magnetic damping of YIG films considerably [14–18]. Ferromagnetic metals and alloys are an alternative category of promising materials that are significantly easier to integrate on-chip. It is therefore desirable to explore and optimize metallic magnets towards low magnetic damping for hybrid magnonic quantum devices [19].

A major contribution to magnetic damping in *metallic* magnets arises from conduction electrons that dissipate magnons through the spin-orbit (SO) interaction [20–22]. This mechanism is described by two early theories, the breathing Fermi surface (BFS) model and the later torque correlation (TC) model that were developed by Kamberský [21,23]. The TC model is more general and describes how the SO torque $\langle n, \mathbf{k}|[\sigma^-, \hat{H}_{SO}]|m, \mathbf{k}\rangle$ induces intraband ($m = n$) and interband ($m \neq n$) electronic transitions which are interpreted as conductivitylike and resistivitylike damping pathways for magnons, respectively [22,24–26]. In its low-scattering limit, when the spectral overlap between different bands is small, damping is largely dominated by the intraband part, in agreement with the BFS model. Damping is shown to be approximately proportional to the electronic density of states (EDOS) at the Fermi level [21,23,27]. Many

*Contact author: schleife@illinois.edu

experimental works confirm that the lowest damping coincides with the lowest EDOS at the Fermi level (EDOS-FL) for ferromagnetic alloys such as cobalt-iron (Co-Fe) and iron-vanadium [28–30]. Therefore, one practical way to reduce magnetic damping is to minimize EDOS-FL by electronic-structure engineering.

In this work, we focus on the paradigmatic ferromagnetic material, body-centered-cubic (bcc) iron. We use first-principles electronic-structure theory to comprehensively study its EDOS-FL under the conditions of (i) thermal atomic disorder, (ii) boron (B) doping, and (iii) structure amorphization. We account for the effect of thermal disorder on EDOS-FL since real devices always work at nonzero temperature, although for superconducting quantum devices the operating temperature can be extremely low. Typical superconducting quantum circuits, such as qubits, are operated at temperatures of a few tens of millikelvins. Meanwhile, recent experimental work has shown that doping carbon or B into ferromagnetic alloys can make the structure amorphous and reduce magnetic damping [31,32]. Hence, it is interesting to investigate the origin of the reduced damping in doped amorphous alloys and the extent to which it can be attributed to reduced EDOS-FL. To explore this, we study the effects of B doping and structure amorphization individually and compare EDOS-FL for *crystalline* Fe doped with B and *amorphous* Fe, as well as *pure crystalline* Fe. Finally, we consider amorphous Fe with B doping to investigate the combined effect.

The remainder of this paper is organized as follows. In Sec. II, we first introduce the methods that are used to construct our simulation cells including bcc Fe supercells with phonon excitations, bcc Fe supercells doped with B, amorphous Fe supercells, and amorphous Fe supercells doped with B. The details of our density functional theory (DFT) simulations are also explained in Sec. II. In Sec. III, we discuss our main results for the EDOS of the different structures. In general, we find that phonon excitations do not significantly change EDOS-FL up to at least 500 K. Doping B into bcc Fe decreases EDOS-FL, while making the Fe amorphous increases EDOS-FL. Overall, amorphous Fe doped with B can have lower EDOS-FL than pure bcc Fe. Finally, we give our conclusions in Sec. IV.

II. METHODOLOGY

Thermal disorder of the atomic positions in the bcc Fe lattice is modeled by considering phonons that displace nuclei from their ideal 0-K lattice positions of the bcc crystal structure [see Fig. 1(a)]. Simulation cells of the thermally disordered lattice are constructed by superimposing harmonic phonon modes with random phases and amplitudes according to classical statistics at different temperatures [34]. In this work, we consider three different temperatures of 10, 300, and 500 K. For each temperature, 50 random snapshots of the disordered $2 \times 2 \times 2$ bcc Fe supercell are generated for simulations. In Fig. 1(b), we show the disordered supercell superimposing 50 snapshots for $T = 300$ K as an example. The supercell snapshots for $T = 10$ K and $T = 500$ K are similar but with different amplitudes of the atomic displacements. For analyzing the EDOS, we average over all 50 snapshots for each temperature.
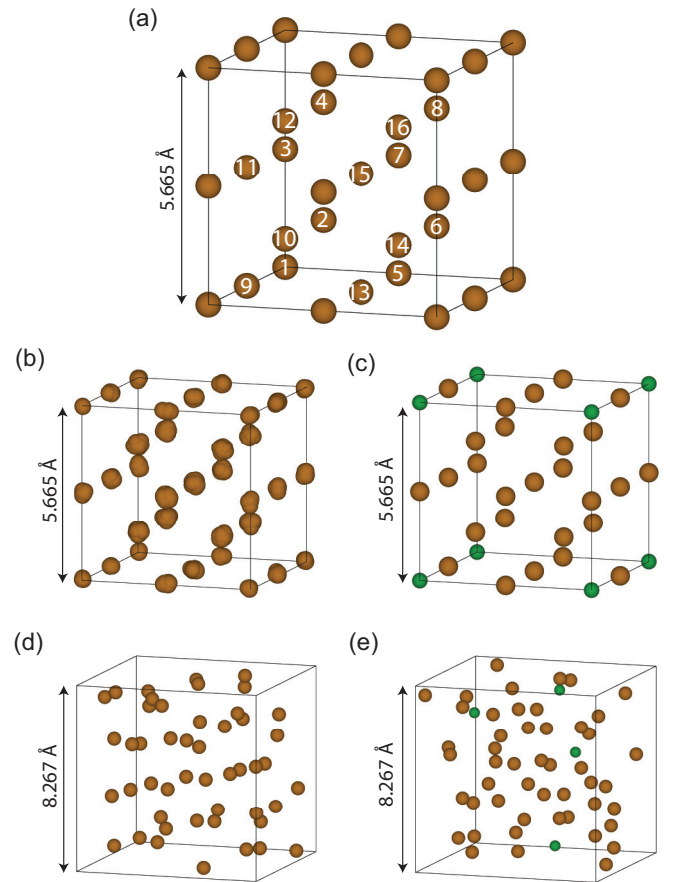

FIG. 1. Simulation supercells used in this work. (a) The $2 \times 2 \times 2$ supercell of ideal bcc Fe at the temperature of $T = 0$ K. The supercell includes 16 Fe atoms (brown spheres) that are labeled by the numbers on them. (b) The bcc Fe supercell at $T = 300$ K, with 50 instantaneous snapshots of the vibrating lattice superimposed. (c) The bcc Fe supercell doped with 6.25% B (green spheres), corresponding to $n_B = 1$ in Table I. (d) Snapshot of amorphous Fe (a-Fe) with a volume of a cubic $3 \times 3 \times 3$ supercell. This supercell is cut from a larger one constructed by molecular dynamics (MD) simulations (see text). (e) Snapshot of amorphous Fe doped with 7.5% B (a-FeB). All these supercell images are produced by VESTA [33].

Lattice geometries for B-doped bcc Fe are constructed using a cluster-expansion method which was used before for studying binary alloys [35–40]. This method starts with a $2 \times 2 \times 2$ bcc Fe supercell with 16 atoms and replaces n_B Fe atoms with B atoms. Generally, there are $C_{n_{Fe}+n_B}^{n_B}$ ways of distributing n_{Fe} Fe atoms and n_B B atoms; however, symmetries of the lattice structure reduce the total number of nonequivalent configurations to a few classes with different folds of degeneracy (see Table I for all different n_B's considered in this paper). Electronic-structure simulations are carried out for only one representative of each class, which significantly reduces the computational effort and allows us to study an alloy with $n_{Fe} + n_B = 16$ atoms. In this work, we consider $n_B = 1$ [see Fig. 1(c) for $Fe_{15}B_1$], 2, 3, and 4 that correspondingly have 1, 4, 6, and 18 nonequivalent classes (see Table I). For each doping level n_B, we compute the EDOS by averaging over the nonequivalent classes weighted by their degeneracies (third column in Table I). There are different methods to

TABLE I. All nonequivalent classes (second column) of arranging n_B B atoms (first column) on 16 Fe bcc lattice sites, $Fe_{16-n_B}B_{n_B}$. Only these representative structures are simulated in our work. The third column provides the degeneracy for each class determined by crystal structure symmetry and the fourth column contains one representative atomic geometry that was used in this work (see atom labels in Fig. 1).

n_B	Class	Degeneracy	Representation
1	1	16	1
2	2	64	1, 2
	3	24	1, 3
	4	24	1, 7
	5	8	1, 15
3	6	192	1, 2, 3
	7	192	1, 2, 7
	8	64	1, 2, 15
	9	48	1, 3, 5
	10	48	1, 3, 13
	11	16	1, 7, 11
4	12	48	1, 2, 3, 4
	13	384	1, 2, 3, 5
	14	96	1, 2, 3, 6
	15	192	1, 2, 3, 8
	16	384	1, 2, 3, 13
	17	96	1, 2, 3, 14
	18	96	1, 2, 3, 16
	19	48	1, 2, 7, 8
	20	128	1, 2, 7, 11
	21	96	1, 2, 7, 12
	22	96	1, 2, 7, 16
	23	16	1, 2, 15, 16
	24	12	1, 3, 5, 7
	25	16	1, 3, 5, 9
	26	48	1, 3, 5, 11
	27	48	1, 3, 5, 15
	28	12	1, 3, 13, 15
	29	4	1, 7, 11, 13

determine the weights used for averaging, introduced in Ref. [35], corresponding to different thermodynamic conditions of the alloy. The weights we use here correspond to a simplification of the strict regular solution, with the macroscopic alloy composition or doping level consisting exclusively of microscopic structures with exactly the same concentration of elements; i.e., we make the assumption that no demixing occurs. Indeed, the phase diagram of Fe-B indicates that the alloy structures may not be stable for the B concentrations studied in this work. However, experimentally we know that B is distributed homogeneously throughout the material in as grown films without postannealing and is kinetically trapped in this configuration [41]. Experimental fabrication of Fe-B films with B concentration ranging from 0% to 30% has been reported recently [42], justifying our choice of atomic configurations. Other computational methods for studying effects of temperature or alloy disorder in materials include the coherent potential approximation (CPA) implemented within the Korringa-Kohn-Rostoker (KKR) formalism [43]. This method has been applied to study the

relation between EDOS and intrinsic magnetic damping for Co-Fe alloys with different Co concentrations [28]. For comparison, we also used our cluster-expansion method to calculate the EDOS of Co-Fe alloys (see details in the Supplemental Material [44]) and found consistent results with the CPA-KKR method.

We construct amorphous Fe (a-Fe) atomic geometries by simulating heating and quenching processes using molecular dynamics (MD) simulations as implemented in the LAMMPS code [45]. The interatomic interactions between Fe atoms are described via a "magnetic" interatomic potential that was developed by Dudarev and Derlet [46–48], based on the embedded atom method. The interatomic potential for our simulation is obtained from the OPENKIM website [49–52]. The same potential has been used previously [53] to generate a-Fe geometries and was shown to produce characteristic features observed in the experimentally measured radial distribution function (RDF) $g(r)$ [54]. In our NVT canonical ensemble MD simulations, we use a $10 \times 10 \times 10$ supercell of bcc Fe with 2000 atoms. The system is then heated to 10 000 K using a Nosé-Hoover thermostat, leading to a completely liquid state. We then implement a cooling process where first the temperature T is decreased to 4000 K in 50 ps and maintained at 4000 K for 250 ps. Subsequently, T is decreased to 3000 K in 250 ps. Finally, T is decreased to 300 K (room temperature) in 50 ps and maintained for another 50 ps. We compute the RDF $g(r)$ for this final structure and find good agreement with the result from Ma *et al.* [53] and the experimental observation from Ichikawa [54] (see Fig. 1 in the Supplemental Material [44]).

We then extract smaller cubic cells from this result, corresponding to volumes of a $3 \times 3 \times 3$ bcc Fe cell [see Fig. 1(d)], and use these for first-principles calculations of the electronic structure. We cut ten such a-Fe snapshots from random positions of the large a-Fe structure, simulate all of them, and average the results. To generate a-Fe doped with B (a-FeB), we use a single a-Fe snapshot and randomly replace Fe atoms by B atoms according to the doping level [see Fig. 1(e)]. For each doping level, ten different configurations of random replacement are constructed for our simulations in order to approach a statistical average.

For all these different atomic geometries, we compute electronic densities of states (EDOS) using DFT as implemented in the Vienna Ab-initio Simulation Package [55,56]. A plane-wave basis with a cutoff energy of 500 eV is applied to expand the Kohn-Sham states. The generalized-gradient approximation parametrized by Perdew, Burke, and Ernzerhof is used for the exchange-correlation functional [57]. All simulations are carried out with spin-polarized DFT which does not include the effect of spin-orbit coupling (SOC). We use different **k**-point grids to sample the Brillouin zone of the different simulation cells: These parameters are determined based on the convergence of the bcc Fe unit-cell for which a $12 \times 12 \times 12$ MP **k**-grid is enough to achieve convergence of the total energy per atom to within 2 meV. For larger supercells, we maintain a similar **k**-grid density by scaling the sampling points inversely with the supercell size. For the supercell of ideal bcc Fe and its thermally disordered lattices, we use a $8 \times 8 \times 8$ Monkhorst-Pack (MP) grid [58]. For the B-doped crystalline Fe structures, $Fe_{n_{Fe}}B_{n_B}$, a $6 \times 6 \times 6$ MP
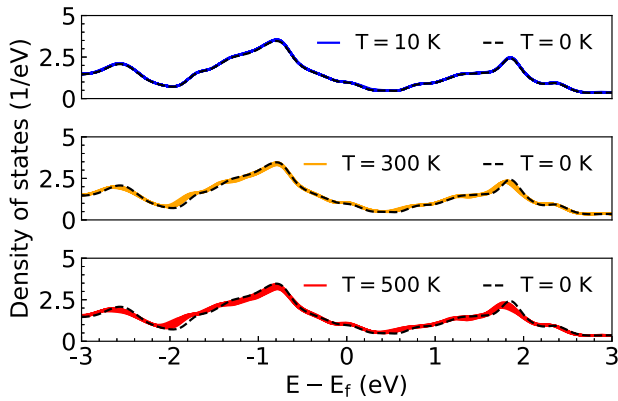
FIG. 2. Electronic density of states (EDOS) of pure Fe, normalized per atom, at different lattice temperatures of $T = 10$ K, 300 K, and 500 K. For each temperature, the EDOS of 50 snapshots is plotted. The EDOS of perfect bcc Fe at $T = 0$ K is included in every subplot for comparison.

grid is applied, and we test that this converges the total energy to within 1 meV/atom. For amorphous structures, we use a $3 \times 3 \times 3$ MP grid. Due to the reduced symmetry of a-Fe, a $4 \times 4 \times 4$ MP **k**-grid is computationally too expensive and we use $3 \times 3 \times 3$ points.

Structural relaxations for ideal bcc Fe and B-doped bcc Fe are performed with a force tolerance of 5 meV/Å. We first relax undoped a-Fe structures within classical MD to a force tolerance of 0.01 eV/Å and refer to these as "MD relaxed" a-Fe. They are then further relaxed by DFT, labeled as "MD + DFT relaxed" a-Fe, with a force tolerance of 0.15 eV/Å, which is the level that we can achieve within a reasonable computational time. We generate B-doped a-Fe from the MD relaxed geometries and relax these within DFT to the same force tolerance of 0.15 eV/Å. Thermally disordered lattices are not relaxed to maintain the frozen snapshots of the vibrating lattice.

III. RESULTS AND DISCUSSION

A. Thermally induced atomic disorder

First, we investigate the effect of finite lattice temperature and the resulting atomic disorder on the EDOS of Fe for temperatures of $T = 10$, 300, and 500 K. Phonon excitations displace nuclei from their equilibrium positions, which increasingly disorders atomic geometries with increasing temperature. The EDOS results for all 50 calculated snapshots are plotted in Fig. 2 for each temperature and compared to the EDOS of ideal bcc Fe at $T = 0$ K.

These results show that increasing the temperature generally broadens the linewidth of the EDOS relative to the zero-temperature counterpart due to the randomness in the atomic positions for the disordered lattice structure. For $T = 300$ and 500 K, noticeable changes to the EDOS are observed especially near peaks at -2.6, -0.8, and 1.8 eV as well as valleys near -2.0 and 0.6 eV (see Fig. 2). While the density of states at the Fermi level $n(E_f)$ (EDOS-FL) is much less affected, we provide a quantitative analysis of these changes since they may directly influence electron-magnon

damping. Towards this, we compute the average and standard deviation of EDOS-FL for each temperature and find for $T = 10$ K that $n(E_f) = 0.991 \pm 0.004$ eV^{-1}, for $T = 300$ K $n(E_f) = 1.038 \pm 0.012$ eV^{-1}, and for $T = 500$ K $n(E_f) = 1.058 \pm 0.019$ eV^{-1}. These three values are all larger than $n(E_f) = 0.974$ eV^{-1} for ideal bcc Fe at zero temperature, showing that increasing temperature increases EDOS-FL for Fe. However, even the increase of about 8.6 % at $T = 500$ K is not significant, compared to the influence of doping and amorphization that we discuss later.

While our results show that EDOS-FL of Fe does not significantly change at low temperatures, this does not imply that magnetic damping is temperature independent, since mechanisms other than conductivitylike damping also contribute. Conductivitylike electron-magnon damping in the intraband scattering limit can be approximately described by the empirical formula $\alpha_{\mathrm{intra}} \sim n(E_f)|\Gamma^-|^2 \tau$ [22,24,59,60], where $|\Gamma^-|$ is the strength of the spin-orbit interaction near the Fermi level and τ is the electron relaxation time, which can be determined from the Drude model or be more precisely calculated from first principles by calculating the self-energy within the alloy analogy model based on the CPA [43]. The proportionality of α_{intra} to the electron relaxation time τ implies that conductivitylike damping [22,24] is more pronounced at lower temperatures or in cleaner crystals where τ is large. This somewhat counterintuitive increase of magnetic damping with increasing τ has been experimentally observed in a recent work on Fe [61] and an earlier work on cobalt and nickel [62]. We note that in this work, we only study the dependence of α_{intra} on $n(E_f)$; however, the relaxation time τ can depend on temperature or other lattice disorders in the crystal, as demonstrated by previous studies [43]. Our simulation results clearly indicate that the EDOS-FL, one of the factors determining the intrinsic magnetic damping in metallic magnets, is not significantly affected by low temperatures. In addition to conductivitylike damping, resistivitylike damping may also be affected by temperature, but is not discussed in this study.

We want to briefly comment on effects of electronic and magnetic temperatures on the EDOS of Fe, although detailed calculations of these are beyond the scope of this paper. Both electronic temperature and magnetic temperature have little effects on the EDOS-FL of Fe [63]. In that work, we computed temperature-dependent (magneto-)optical spectra of Fe and quantified the influence of electronic and magnetic temperature on optical transitions and optical spectra.

B. Boron doping

Next, we compare the EDOS of bcc Fe doped with B to that of pure bcc Fe. Four different doping levels are considered and modeled by the structures Fe$_{15}$B$_1$ (6.25% B), Fe$_{14}$B$_2$ (12.5% B), Fe$_{13}$B$_3$ (18.75% B), and Fe$_{12}$B$_4$ (25% B), constructed using the cluster expansion method (see Sec. II). Except for the case $n_{\mathrm{B}} = 1$ which is represented by only one class, we calculate weighted averages and standard deviations (error bar) over all classes in Table I for the other doping levels.

We find that doping B into bcc Fe leads to a reduced EDOS-FL compared to the pure bcc Fe for all doping levels
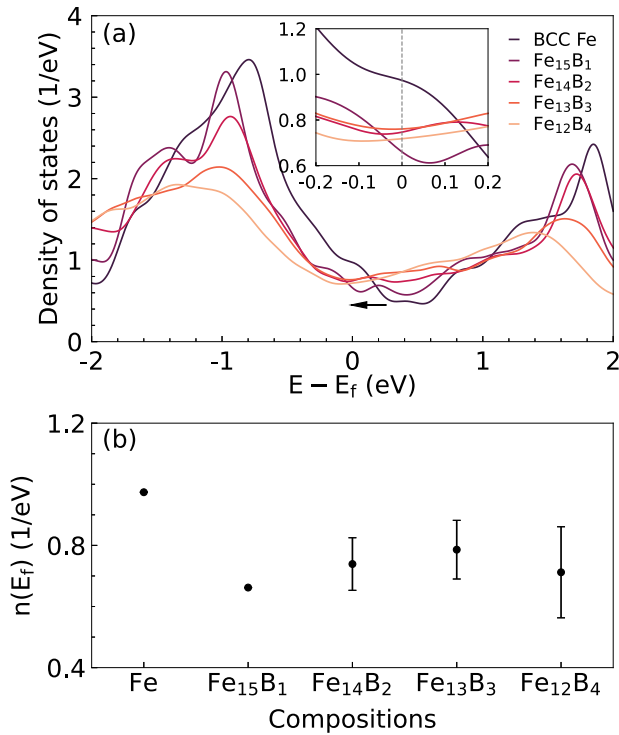
FIG. 3. (a) EDOS, normalized per atom, for Fe and Fe doped with B, simulated using a $2 \times 2 \times 2$ supercell with different numbers of B atoms, $Fe_{16-n_B}B_{n_B}$, for $n_B = 1, 2, 3,$ and 4. Cluster expansion averages are shown for $n_B > 1$. The inset magnifies EDOS-FL and clearly shows a reduction by B doping. (b) Average and error bar of EDOS-FL for different doping concentrations of $Fe_{16-n_B}B_{n_B}$. For pure Fe and $Fe_{15}B_1$ only one nonequivalent class (see Table I) is used and, thus, we compute no standard deviation.

FIG. 4. (a) Ground-state total energy E_0 in eV, (b) magnetic moment m in μ_B, and (c) electronic density of states at the Fermi level, $n(E_f)$, normalized per atom, for all 18 nonequivalent classes corresponding to the structure $Fe_{12}B_4$ (see Table I). The horizontal dashed line in panel (c) indicates $n(E_f)$ for pure bcc Fe.

considered here [see Fig. 3(a)]. This is because doping with B shifts the entire EDOS to lower energies, such that the Fermi level shifts to the dip in the original nondoped EDOS, as indicated by the black arrow in Fig. 3(a). Main peaks in the EDOS, i.e., at -0.784 and 1.853 eV, are also shifted to lower energies with increasing B doping. Meanwhile, peak intensities are decreased and peaks widths are broadened with increasing B doping.

Our data also point to a nonmonotonic dependence of $n(E_f)$ on the B-doping concentration and, as a result, the possibility of optimizing the doping level to minimize magnon damping. Figure 3(b) shows the average value and the error bar for different doped systems and pure bcc Fe. Our results indicate an optimal B doping level of 6.25%, which leads to the lowest $n(E_f) = 0.662$ eV^{-1}. At the same time, with increasing the number of B atoms in the doped cell, there are more nonequivalent classes as seen from Table I, and the error bar increases from $n_B = 2$ to $n_B = 4$. In particular, the EDOS-FL for $Fe_{12}B_4$ has a large error bar, which implies that the values of $n(E_f)$ for the 18 nonequivalent classes (see Table I) spread over a large range. These classes, although having the same composition, are microscopically quite different regarding the distribution of B on the Fe lattice. In Fig. 4, we analyze the ground-state total energy E_0, the magnetic moment $\mathbf{m}$, and the EDOS-FL $n(E_f)$ for the 18 nonequivalent classes. While $n(E_f)$ spans over a big range from 0.327 to 1.030 eV^{-1}, all
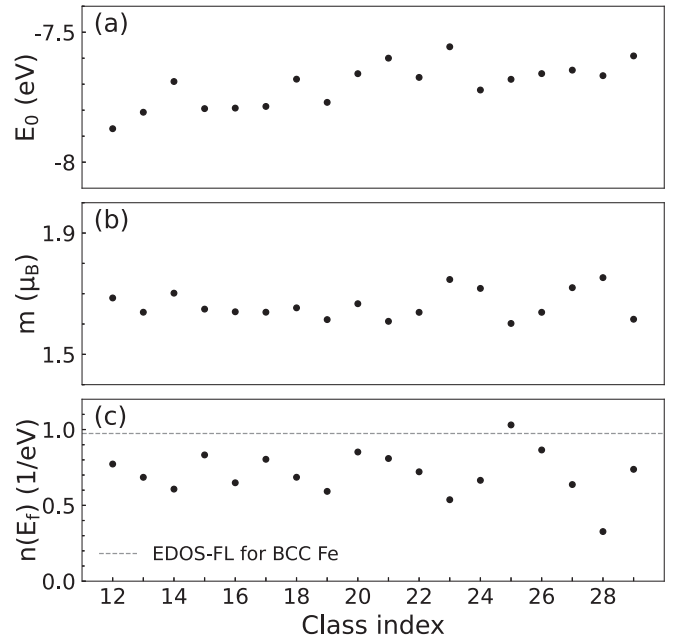
values remain smaller than the value of the pure bcc Fe, except for the class with the index 25 (see Table I). This confirms that doping B still decreases EDOS-FL in general. The difference between maximum and minimum values of E_0, $\mathbf{m}$, and $n(E_f)$ amounts to 4.09%, 9.08%, and 98.74%, respectively, relative to their average values. We do not identify obvious correlation between the total energy and the EDOS-FL in Fig. 4, with a correlation coefficient of -0.110. For the lowest-energy class with an index of $n = 12$, $n(E_f) = 0.772$ eV^{-1}, which is larger than the average, while the class with an index of 28 has a relatively large energy, but the lowest EDOS-FL. However, we do find a noticeable negative correlation between the magnetic moment and the EDOS-FL with a correlation coefficient of -0.683. This observation is beneficial for real magnetic devices, where lower magnetic damping and higher magnetization is often desirable for applications. In fact, the saturation magnetization M_s is related to the effective damping field in the Landau-Lifshitz-Gilbert equation [64] as $\mathbf{H} \propto \frac{1}{M_s}$ demonstrated by previous theoretical studies [25]. It could also suggest that growing B-doped Fe under an external magnetic field, and thus making high magnetic moment atomic geometries more likely, could lead to samples with lower magnetic damping. It is already well established that synthesis or annealing of amorphous ferromagnets in applied magnetic fields may lead to induced magnetic anisotropies due to modifications of the short-range order [65]. Similarly, it is conceivable that applying fields during growth or during a postannealing may stabilize larger saturation magnetizations [66].

We address two more points regarding the study of B-doped Fe structures to end this section. First, although in this work we focus on B-doped Fe by substitution, for which

we provide a comprehensive investigation of configurational disorder by means of a cluster expansion, it is reasonable to consider other defect atomic geometries such as interstitials, as suggested by previous studies [67]. To compare the difference between these two scenarios, we construct a structure with one B atom occupying an octahedral interstitial site in the $2 \times 2 \times 2$ bcc Fe supercell [67] and calculate its EDOS. Interestingly, this structure also shows a decreased EDOS-FL compared to the pure bcc Fe (see details in the Supplmental Material [44]), indicating reduced intrinsic magnetic damping from conduction electrons. Moreover, this result also qualitatively agrees with experimental measurements for B-doped Co-Fe alloys where doping B reduced magnetic relaxation [67]. Second, aside from the changes of the EDOS, we notice that neither spin DOS for Fe has a gap, and as a result, a half-metallic state with even lower magnetic damping would not be achieved via B doping. Doping with B may, however, lower the Curie temperature of the magnetic material due to introducing nonmagnetic elements. Such a reduction would not be of concern for applications, as experimentally it is known that the Curie temperature of B-doped Co-Fe alloys is well above room temperature even for relatively high boron concentrations exceeding 20% [32,68]. Lastly, increasing B doping will reduce the magnetic anisotropy because it drives the structural phase transition to amorphous structures according to experimental observations [32].

C. Structure amorphization

Next, we study the influence of structure amorphization by characterizing a-Fe via the radial distribution function (RDF) $g(r)$. As explained in Sec. II, we use molecular dynamics (MD) to compute atomic positions for a large a-Fe supercell, from which we randomly cut ten small cubic cells [see the yellow box in Fig. 5(a)] and subsequently relax using MD (MD-relaxed) or MD and DFT (MD + DFT relaxed). For eight of these cells, MD and DFT relaxation does not change the RDF and maintains amorphousness, while the other two relax and recrystallize, as evidenced by their RDF. This is shown in Fig. 5(b) for one representative a-Fe cell for which relaxation does not change the amorphousness but simply smoothens $g(r)$. In contrast, Fig. 5(c) shows one example for which DFT relaxation recrystallizes the amorphous structure and discrete sharp peaks appear that coincide with the RDF of ideal bcc Fe. For our purpose of studying EDOS-FL for a-Fe, we exclude the two recrystallized samples. The averaged RDF of the remaining eight a-Fe cells is calculated and compared in Fig. 5(d) to the RDF of the large initial a-Fe supercell, depicted in Fig. 5(a). We can see that for large r they almost overlap. For small r around 2.5 Å, the two curves slightly differ, but still show similar peak structures. Based on this, we conclude that the average of the small a-Fe cells approximates the large a-Fe cell well enough to study EDOS-FL for a-Fe.

Figure 6 shows that a-Fe has a broadened distribution of the average EDOS and an increased value of the EDOS-FL, compared to the ideal bcc Fe. The peak structure of the EDOS of bcc Fe is lost for a-Fe and the entire EDOS is smoother and broadened. We note that performing a DFT relaxation on top of the MD relaxed structure can decrease $n(E_f)$ values even further (see Fig. 6). However, the increase of EDOS-FL
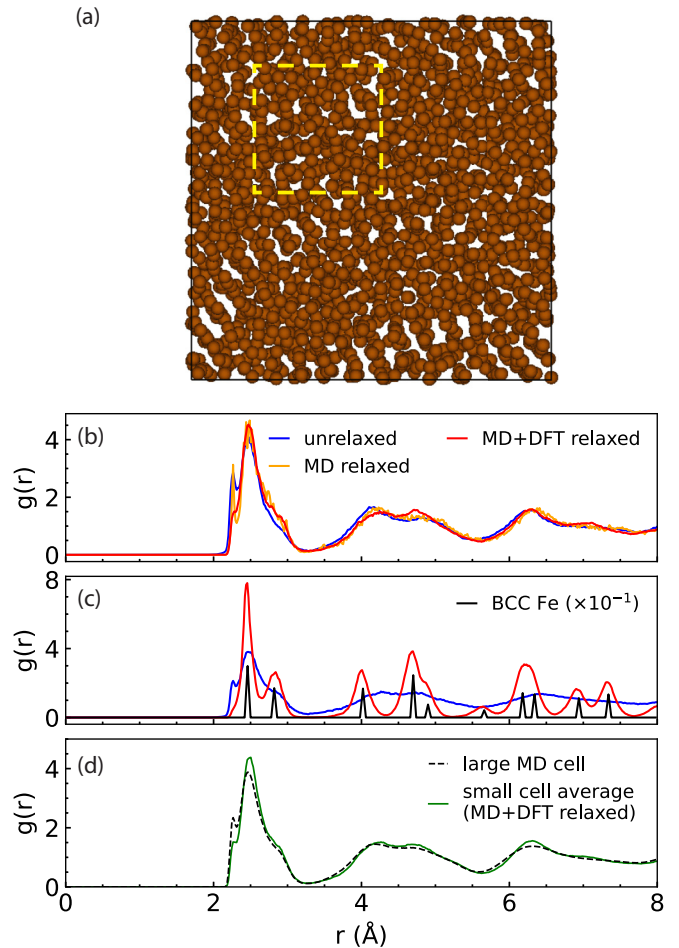

FIG. 5. a-Fe structure and the RDF $g(r)$. (a) Illustration of the large cubic a-Fe supercell constructed by MD. The yellow dashed box shows a small cubic a-Fe cell cut out for DFT simulations. (b) One representative small a-Fe cell for which DFT relaxation does not change the RDF away from the amorphous state. (c) One representative small a-Fe cell for which DFT relaxation leads to recrystallization, i.e., the RDF approaches the RDF of ideal bcc Fe. (d) RDF for the large a-Fe cell created from MD, compared to the average $g(r)$ of eight small a-Fe cells that are randomly cut from it.
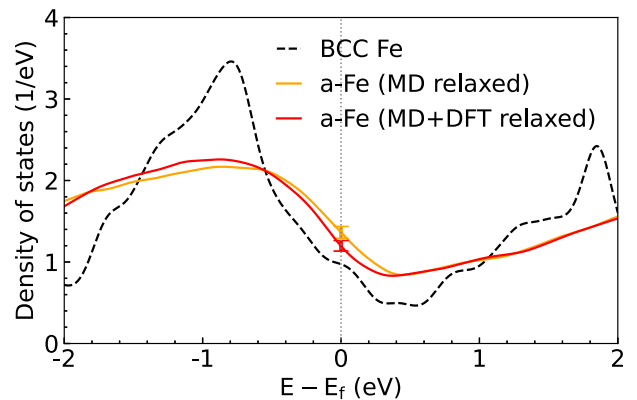

FIG. 6. EDOS, normalized per atom, averaged over eight simulation cells for a-Fe. EDOS-FL increases for both the MD relaxed structures and MD + DFT relaxed structures, relative to ideal Fe. The error bar is computed from the standard deviation.

for a-Fe is larger than the error bar for both structure relaxation approaches. Since DFT relaxations with tight force convergence criteria are computationally expensive, we do not explore this in more detail in this work. Instead, we conclude that it is not desirable to reduce $n(E_f)$ values of Fe by structure amorphization.

Finally, our $g(r)$ results illustrate that the a-Fe structure generated from our MD simulations is fundamentally different from the Fe structure up to a temperature of $T = 500$ K, even though in both cases the original perfect bcc Fe lattice structure is appreciably disordered (see details in Fig. S2 of the Supplemental Material [44]). Comparing to the $g(r)$ of the perfect bcc Fe at zero lattice temperature, the temperature-induced disorder just broadens the original peaks. Some individual peaks are merged if they are too close to each other along the r axis. The a-Fe structure, however, has a fundamentally different $g(r)$. A new distinct peak appears below the lowest interatomic distance of bcc Fe, which is even lying outside the broadening observed for $T = 500$ K. Meanwhile, $g(r)$ for larger r has a nearly continuous distribution instead of a discrete distribution sharply peaked at specific distances. This is consistent with our result of only a minor influence of lattice temperature on EDOS-FL and a more noticeable change for a-Fe.

D. Amorphous iron with boron doping

Finally, after showing in Sec. III B that B doping can decrease the electronic density of states at the Fermi level (EDOS-FL) for *crystalline* Fe, we now consider B doping of a-Fe. For each doping level, the random distribution of B sites is considered by calculating ten possible configurations. They are constructed as described in Sec. II and subsequently relaxed using DFT until forces on all atoms are smaller than 0.15 eV/Å, i.e., the same force tolerance used for MD + DFT relaxed a-Fe. For each of these the EDOS is computed and averaged for analysis.

Our results in Fig. 7(a) show that B doping decreases the averaged EDOS at the Fermi level $n(E_f)$ (EDOS-FL) for a-FeB, similar to what we observed for crystalline bcc Fe. With increasing B doping, the EDOS-FL of a-FeB monotonically decreases in the range from 0% to 18.9% B and starts to saturate around 15%. The inset in Fig. 7(a) focuses on this trend near the Fermi energy (see the black arrow). Interestingly, doping B into a-Fe can lead to an EDOS-FL that is even smaller than that of the pure bcc Fe, overcoming the increase we discussed for a-Fe (see Fig. 6). This implies that a-FeB is potentially advantageous for reducing intrinsic intraband magnon-electron damping, even though undoped a-Fe is not. The change of EDOS-FL in a-FeB versus B doping level observed here qualitatively matches the change of measured magnetic damping versus B concentration in Fe-B films reported from a recent experiment [42].

This is illustrated more clearly in Fig. 7(b) via averages and standard deviations. The decrease of $n(E_f)$ with increasing B doping from 0% to 18.9% is outside the statistical error bars and gradually saturates when the doping percentage is $\gtrsim 15\%$. Therefore, we do not consider larger doping percentages in this work. It is possible that further increasing the doping percentage may even increase $n(E_f)$ similar to what we have
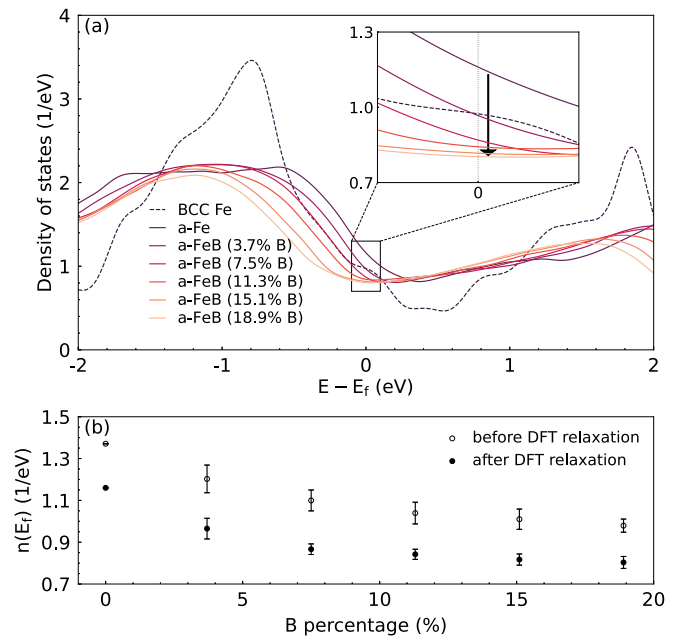

FIG. 7. (a) EDOS per atom for ideal bcc Fe (same data as in Fig. 3), a-Fe (the single snapshot used to build doped a-Fe through random replacement), and a-FeB (B doped a-Fe) with different doping levels of 3.7%, 7.5%, 11.3%, 15.1%, and 18.9%. For each doping level of a-FeB the plotted result is the average over ten different snapshots with random replacements of Fe atoms by B atoms, starting from a single original a-Fe supercell. The inset magnifies the EDOS near the Fermi level. (b) Averages and standard deviations of EDOS-FL for different levels of B doping. Results before DFT relaxation are shown for comparison.

observed for B-doped bcc Fe in Fig. 3(b). Exploring this is outside the scope of this work, since it does not lead to reduced magnetic damping. Our simulations indicate that 18.9% of B doping is near the optimal doping level that corresponds to the lowest $n(E_f)$ for a-FeB.

Finally, for all simulated a-FeB structures, DFT relaxation leads to a reduction of the EDOS-FL, similar to what we observed for a-Fe in Fig. 6. Figure 7(b) shows for different B-doping percentages that this reduction is beyond the range of the statistical error bar. The trend in this figure indicates that while relaxing the amorphous structure to even lower force tolerance is computationally costly, it could lead to slightly lower values of the EDOS-FL.

We summarize our numerical results for averages and standard deviations of the EDOS-FL for all simulated structures in Table II. This shows that crystalline bcc Fe doped with 6.25% B leads to the lowest EDOS-FL among all structures considered. Previous experimental work has demonstrated that doping carbon into Co-Fe alloys can naturally make the structure amorphous and that amorphous Co-Fe-C alloys can have magnetic damping smaller than that of polycrystalline Co-Fe alloys [31]. Recent experiments have confirmed that similar effects can be achieved with B doping [32,42]. While this is explained by smaller grain sizes in the amorphous material and, therefore, reduced sample inhomogeneity leading to lower damping, our results indicate that B doping of amorphous Fe is an additional factor that can reduce the

TABLE II. Electron density of states of bcc Fe at the Fermi level (EDOS-FL) for all different structures studied in this work, i.e., nonzero lattice temperature, B doping, amorphous lattice (a-Fe), and B-doped amorphous Fe (a-FeB). Values are normalized per atom and we report averages and standard deviations for the cases where multiple configurations contribute (see text).

Structures		EDOS-FL (1/eV)	Error
bcc Fe	$T = 0$ K	0.974	—
	$T = 10$ K	0.991	0.004
	$T = 300$ K	1.038	0.012
	$T = 500$ K	1.058	0.019
B-doped bcc Fe	6.25% B	0.662	—
	12.50% B	0.746	0.068
	18.75% B	0.760	0.059
	25.00% B	0.718	0.094
a-Fe		1.199	0.065
a-FeB	3.7% B	0.965	0.049
	7.5% B	0.866	0.025
	11.3% B	0.842	0.024
	15.1% B	0.817	0.027
	18.9% B	0.803	0.029

intrinsic magnetic damping by decreasing the EDOS-FL. Lastly, we want to point out that magnetic damping is in general nonlocal and anisotropic, as demonstrated by previous studies [26,59,69]. However, current hybrid magnonic quantum devices use mostly the uniform magnon modes ($k = 0$) that are the focus of this work and for these nonlocality is less important. Magnetic damping can also be highly anisotropic, which has been revealed both theoretically [26] and experimentally [59,69]. Such anisotropy can come from anisotropic SOC [59] or anisotropic EDOS-FL [69]. We plan to investigate this in more detail in future work on magnetic damping of propagating magnons.

IV. CONCLUSIONS

We used first-principles simulations to quantitatively study the influence of lattice temperature, boron doping, and structure amorphization on the electronic structure of iron. Using our results, we discussed how these factors affect the electronic density of states at the Fermi level, as one important quantity determining the intrinsic magnetic damping in metallic magnets within Kamberský's breathing Fermi surface model. Generally, we showed that both structural effects modify the density of states near the Fermi level to a lesser extent. Instead, doping with B is advantageous in crystalline and amorphous Fe to reduce damping and an optimal doping level of 6.25% B reduces the EDOS-FL by 32% in crystalline Fe. We also showed that different arrangements of the B atoms on Fe sites affect the resulting magnetization and EDOS-FL values differently. This possibly suggests materials growth under an external magnetic field to favor arrangements with large magnetization and small damping. While this work points to a reduction of the EDOS-FL as one reason for reduced magnetic damping in B-doped Fe, we expect similar mechanisms to govern C-doped material and Co-Fe alloys.

[1] Y. Li, W. Zhang, V. Tyberkevych, W. K. Kwok, A. Hoffmann, and V. Novosad, Hybrid magnonics: Physics, circuits, and applications for coherent information processing, J. Appl. Phys. **128**, 130902 (2020).

[2] D. D. Awschalom, C. R. Du, R. He, F. J. Heremans, A. Hoffmann, J. Hou, H. Kurebayashi, Y. Li, L. Liu, V. Novosad, J. Sklenar, S. E. Sullivan, D. Sun, H. Tang, V. Tyberkevych, C. Trevillian, A. W. Tsen, L. R. Weiss, W. Zhang, X. Zhang *et al.*, Quantum engineering with hybrid magnonic systems and materials, IEEE Trans. Quantum Eng. **2**, 1 (2021).

[3] H. Y. Yuan, Y. Cao, A. Kamra, R. A. Duine, and P. Yan, Quantum magnonics: When magnon spintronics meets quantum information science, Phys. Rep. **965**, 1 (2022).

[4] Z. Jiang, J. Lim, Y. Li, W. Pfaff, T.-H. Lo, J. Qian, A. Schleife, J.-M. Zuo, V. Novosad, and A. Hoffmann, Integrating magnons for quantum information, Appl. Phys. Lett. **123**, 130501 (2023).

[5] Y. Tabuchi, S. Ishino, A. Noguchi, T. Ishikawa, R. Yamazaki, K. Usami, and Y. Nakamura, Coherent coupling between a ferromagnetic magnon and a superconducting qubit, Science **349**, 405 (2015).

[6] S. M. Rezende, *Fundamentals of Magnonics*, Lecture Notes in Physics Vol. 969 (Springer, Cham, 2020).

[7] N. Kostylev, M. Goryachev, and M. E. Tobar, Superstrong coupling of a microwave cavity to yttrium iron garnet magnons, Appl. Phys. Lett. **108**, 062402 (2016).

[8] B. Bhoi, T. Cliff, I. S. Maksymov, M. Kostylev, R. Aiyar, N. Venkataramani, S. Prasad, and R. L. Stamps, Study of photon-magnon coupling in a YIG-film split-ring resonant system, J. Appl. Phys. **116**, 243906 (2014).

[9] Y. Li, T. Polakovic, Y. L. Wang, J. Xu, S. Lendinez, Z. Zhang, J. Ding, T. Khaire, H. Saglam, R. Divan, J. Pearson, W. K. Kwok, Z. Xiao, V. Novosad, A. Hoffmann, and W. Zhang, Strong coupling between magnons and microwave photons in on-chip ferromagnet-superconductor thin-film devices, Phys. Rev. Lett. **123**, 107701 (2019).

[10] J. T. Hou and L. Liu, Strong coupling between microwave photons and nanomagnet magnons, Phys. Rev. Lett. **123**, 107702 (2019).

[11] G. Schmidt, C. Hauser, P. Trempler, M. Paleschke, and E. T. Papaioannou, Ultra thin films of yttrium iron garnet with very low damping: A review, Phys. Status Solidi B **257**, 1900644 (2020).

[12] H. L. Glass and M. T. Elliot, Attainment of the intrinsic FMR linewidth in yttrium iron garnet films grown by liquid phase epitaxy, J. Cryst. Growth **34**, 285 (1976).

[13] A. Hirohata, K. Yamada, Y. Nakatani, L. Prejbeanu, B. Diény, P. Pirro, and B. Hillebrands, Review on spintronics: Principles and device applications, J. Magn. Magn. Mater. **509**, 166711 (2020).

[14] C. L. Jermain, S. V. Aradhya, N. D. Reynolds, R. A. Buhrman, J. T. Brangham, M. R. Page, P. C. Hammel, F. Y. Yang, and D. C. Ralph, Increased low-temperature damping in yttrium iron garnet thin films, Phys. Rev. B **95**, 174411 (2017).

[15] V. Danilov, D. Lyfar', Y. V. Lyubon'ko, A. Y. Nechiporuk, and S. Ryabchenko, Low-temperature ferromagnetic resonance in epitaxial garnet films on paramagnetic substrates, Sov. Phys. J. **32**, 276 (1989).

[16] V. Danilov and A. Y. Nechiporuk, Experimental investigation of the quantum amplification effect for magnetostatic waves in ferrite-paramagnet structures, Tech. Phys. Lett. **28**, 369 (2002).

[17] L. Mihalceanu, V. I. Vasyuchka, D. A. Bozhko, T. Langner, A. Y. Nechiporuk, V. F. Romanyuk, B. Hillebrands, and A. A. Serga, Temperature-dependent relaxation of dipole-exchange magnons in yttrium iron garnet films, Phys. Rev. B **97**, 214405 (2018).

[18] S. Kosen, A. F. van Loo, D. A. Bozhko, L. Mihalceanu, and A. D. Karenowska, Microwave magnon damping in YIG films at millikelvin temperatures, APL Mater. **7**, 101120 (2019).

[19] S. Azzawi, A. Umerski, L. C. Sampaio, S. A. Bunyaev, G. N. Kakazei, and D. Atkinson, Synthetic route to low damping in ferromagnetic thin-films, APL Mater. **11**, 081108 (2023).

[20] V. Korenman and R. E. Prange, Anomalous damping of spin waves in magnetic metals, Phys. Rev. B **6**, 2769 (1972).

[21] V. Kamberský, On ferromagnetic resonance damping in metals, Czech. J. Phys. **26**, 1366 (1976).

[22] K. Gilmore, Y. U. Idzerda, and M. D. Stiles, Identification of the dominant precession-damping mechanism in Fe, Co, and Ni by first-principles calculations, Phys. Rev. Lett. **99**, 027204 (2007).

[23] V. Kamberský, On the Landau–Lifshitz relaxation in ferromagnetic metals, Can. J. Phys. **48**, 2906 (1970).

[24] V. Kamberský, Spin-orbital Gilbert damping in common magnetic metals, Phys. Rev. B **76**, 134416 (2007).

[25] K. Gilmore, Y. U. Idzerda, and M. D. Stiles, Spin-orbit precession damping in transition metal ferromagnets (invited), J. Appl. Phys. **103**, 07D303 (2008).

[26] D. Thonig and J. Henk, Gilbert damping tensor within the breathing Fermi surface model: anisotropy and non-locality, New J. Phys. **16**, 013032 (2014).

[27] S. Mizukami, F. Wu, A. Sakuma, J. Walowski, D. Watanabe, T. Kubota, X. Zhang, H. Naganuma, M. Oogane, Y. Ando, and T. Miyazaki, Long-lived ultrafast spin precession in manganese alloys films with a large perpendicular magnetic anisotropy, Phys. Rev. Lett. **106**, 117201 (2011).

[28] M. A. Schoen, D. Thonig, M. L. Schneider, T. J. Silva, H. T. Nembach, O. Eriksson, O. Karis, and J. M. Shaw, Ultra-low

magnetic damping of a metallic ferromagnet, Nat. Phys. **12**, 839 (2016).

[29] M. A. W. Schoen, J. Lucassen, H. T. Nembach, B. Koopmans, T. J. Silva, C. H. Back, and J. M. Shaw, Magnetic properties in ultrathin 3d transition-metal binary alloys. II. Experimental verification of quantitative theories of damping and spin pumping, Phys. Rev. B **95**, 134411 (2017).

[30] M. Arora, E. K. Delczeg-Czirjak, G. Riley, T. J. Silva, H. T. Nembach, O. Eriksson, and J. M. Shaw, Magnetic damping in polycrystalline thin-film Fe-V alloys, Phys. Rev. Appl. **15**, 054031 (2021).

[31] J. Wang, C. Dong, Y. Wei, X. Lin, B. Athey, Y. Chen, A. Winter, G. M. Stephen, D. Heiman, Y. He, H. Chen, X. Liang, C. Yu, Y. Zhang, E. J. Podlaha-Murphy, M. Zhu, X. Wang, J. Ni, M. McConney, J. Jones *et al.*, Magnetostriction, soft magnetism, and microwave properties in Co-Fe-C alloy films, Phys. Rev. Appl. **12**, 034011 (2019).

[32] J. Lourembam, K. H. Khoo, J. Qiu, H. Xie, S. K. Wong, Q. J. Yap, and S. T. Lim, Tuning damping and magnetic anisotropy in ultrathin boron-engineered MgO/Co–Fe–B/MgO heterostructures, Adv. Electron. Mater. **7**, 2100351 (2021).

[33] K. Momma and F. Izumi, Vesta 3 for three-dimensional visualization of crystal, volumetric and morphology data, J. Appl. Crystallogr. **44**, 1272 (2011).

[34] D. Åberg, P. Erhart, and V. Lordi, Contributions of point defects, chemical disorder, and thermal vibrations to electronic properties of $Cd_{1-x}Zn_xTe$ alloys, Phys. Rev. B **88**, 045201 (2013).

[35] A. Schleife, M. Eisenacher, C. Rödl, F. Fuchs, J. Furthmüller, and F. Bechstedt, *Ab initio* description of heterostructural alloys: Thermodynamic and structural properties of $Mg_xZn_{1-x}O$ and $Cd_xZn_{1-x}O$, Phys. Rev. B **81**, 245210 (2010).

[36] A. Schleife, C. Rödl, J. Furthmüller, and F. Bechstedt, Electronic and optical properties of $Mg_xZn_{1-x}O$ and $Cd_xZn_{1-x}O$ from *ab initio* calculations, New J. Phys. **13**, 085012 (2011).

[37] J. M. Sanchez, F. Ducastelle, and D. Gratias, Generalized cluster description of multicomponent systems, Phys. A (Amsterdam, Neth.) **128**, 334 (1984).

[38] A. Zunger, in *Statistics and Dynamics of Alloy Phase Transformations*, edited by P. E. A. Turchi and A. Gonis (Plenum Press, New York, 1994), p. 361.

[39] L. K. Teles, J. Furthmüller, L. M. R. Scolfaro, J. R. Leite, and F. Bechstedt, First-principles calculations of the thermodynamic and structural properties of strained $In_xGa_{1-x}N$ and $Al_xGa_{1-x}N$ alloys, Phys. Rev. B **62**, 2475 (2000).

[40] C. Caetano, L. K. Teles, M. Marques, A. Dal Pino, and L. G. Ferreira, Phase stability, chemical bonds, and gap bowing of $In_xGa_{1-x}N$ alloys: Comparison between cubic and wurtzite structures, Phys. Rev. B **74**, 045215 (2006).

[41] T. Miyajima, T. Ibusuki, S. Umehara, M. Sato, S. Eguchi, M. Tsukada, and Y. Kataoka, Transmission electron microscopy study on the crystallization and boron distribution of CoFeB/MgO/CoFeB magnetic tunnel junctions with various capping layers, Appl. Phys. Lett. **94**, 122501 (2009).

[42] M. M. Qaid, C. Ballani, F. Syrowatka, T. Peters, G. Reiss, G. Buettel, U. Hartmann, and G. Schmidt, Tunable Gilbert damping and magnetization in B-rich $Fe_{1-x}B_x$ thin films, Phys. Rev. Mater. **8**, 034404 (2024).

[43] H. Ebert, S. Mankovsky, K. Chadova, S. Polesya, J. Minár, and D. Ködderitzsch, Calculating linear-response functions for

finite temperatures on the basis of the alloy analogy model, Phys. Rev. B **91**, 165132 (2015).

[44] See Supplemental Material at http://link.aps.org/supplemental/10.1103/PhysRevB.109.235147 for the radial distribution function of amorphous iron; different microscopic structures for $Fe_{12}B_4$; the EDOS for cobalt-iron alloys; the spin density of states of boron-doped iron; the EDOS of iron doped with interstitial boron atoms; a comparison of radial distribution function of amorphous iron to bcc iron at different temperatures, which also includes Ref. [70].

[45] A. P. Thompson, H. M. Aktulga, R. Berger, D. S. Bolintineanu, W. M. Brown, P. S. Crozier, P. J. in 't Veld, A. Kohlmeyer, S. G. Moore, T. D. Nguyen, R. Shan, M. J. Stevens, J. Tranchida, C. Trott, and S. J. Plimpton, LAMMPS - a flexible simulation tool for particle-based materials modeling at the atomic, meso, and continuum scales, Comput. Phys. Commun. **271**, 108171 (2022).

[46] S. L. Dudarev and P. M. Derlet, A magnetic interatomic potential for molecular dynamics simulations, J. Phys.: Condens. Matter **17**, 7097 (2005).

[47] S. L. Dudarev and P. M. Derlet, A 'magnetic' interatomic potential for molecular dynamics simulations, J. Phys.: Condens. Matter **19**, 239001 (2007).

[48] P. M. Derlet and S. L. Dudarev, Million-atom molecular dynamics simulations of magnetic iron, Prog. Mater. Sci. **52**, 299 (2007).

[49] R. S. Elliott and E. B. Tadmor, Knowledge base of interatomic models (KIM) application programming interface (API), https://openkim.org/kim-api (2011).

[50] E. B. Tadmor, R. S. Elliott, J. P. Sethna, R. E. Miller, and C. A. Becker, The potential of atomistic simulations and the knowledgebase of interatomic models, JOM **63**, 17 (2011).

[51] M. R. Gilbert, EAM potential for magnetic bcc metals with cubic spline interpolation v002, OpenKIM, https://doi.org/10.25950/9776664f (2018).

[52] S. Dudarev and P. Derlet, EAM potential (magnetic, cubic tabulation) for magnetic Fe developed by Dudarev and Derlet (2005) v002, OpenKIM, https://doi.org/10.25950/eb4996de (2018).

[53] P. W. Ma, W. C. Liu, C. H. Woo, and S. L. Dudarev, Large-scale molecular dynamics simulation of magnetic properties of amorphous iron under pressure, J. Appl. Phys. **101**, 073908 (2007).

[54] T. Ichikawa, Electron diffraction study of the local atomic arrangement in amorphous iron and nickel films, Phys. Status Solidi A **19**, 707 (1973).

[55] G. Kresse and J. Furthmüller, Efficiency of ab-initio total energy calculations for metals and semiconductors using a plane-wave basis set, Comput. Mater. Sci. **6**, 15 (1996).

[56] G. Kresse and J. Furthmüller, Efficient iterative schemes for *ab initio* total-energy calculations using a plane-wave basis set, Phys. Rev. B **54**, 11169 (1996).

[57] J. P. Perdew, K. Burke, and M. Ernzerhof, Generalized gradient approximation made simple, Phys. Rev. Lett. **77**, 3865 (1996).

[58] H. J. Monkhorst and J. D. Pack, Special points for Brillouinzone integrations, Phys. Rev. B **13**, 5188 (1976).

[59] Y. Li, F. Zeng, S. S.-L. Zhang, H. Shin, H. Saglam, V. Karakas, O. Ozatay, J. E. Pearson, O. G. Heinonen, Y. Wu, A. Hoffmann, and W. Zhang, Giant anisotropy of Gilbert damping in epitaxial CoFe films, Phys. Rev. Lett. **122**, 117203 (2019).

[60] M. Fähnle, D. Steiauf, and J. Seib, The Gilbert equation revisited: anisotropic and nonlocal damping of magnetization dynamics, J. Phys. D **41**, 164014 (2008).

[61] B. Khodadadi, A. Rai, A. Sapkota, A. Srivastava, B. Nepal, Y. Lim, D. A. Smith, C. Mewes, S. Budhathoki, A. J. Hauser, M. Gao, J. F. Li, D. D. Viehlad, Z. Jiag, J. J. Heremas, P. V. Balachadra, T. Mewes, and S. Emori, Conductivitylike Gilbert damping due to intraband scattering in epitaxial iron, Phys. Rev. Lett. **124**, 157201 (2020).

[62] S. M. Bhagat and P. Lubitz, Temperature variation of ferromagnetic relaxation in the 3*d* transition metals, Phys. Rev. B **10**, 179 (1974).

[63] K. Kang, D. G. Cahill, and A. Schleife, Temperature-dependent optical and magneto-optical spectra of ferromagnetic BCC Fe, arXiv:2404.03545.

[64] T. L. Gilbert, A phenomenological theory of damping in ferromagnetic materials, IEEE Trans. Magn. **40**, 3443 (2004).

[65] B. S. Berry and W. C. Pritchet, Magnetic annealing and directional ordering of an amorphous ferromagnetic alloy, Phys. Rev. Lett. **34**, 1022 (1975).

[66] C. Wu, K. Wang, D. Li, C. Lou, Y. Zhao, Y. Gao, and Q. Wang, Tuning microstructure and magnetic properties of electrodeposited CoNiP films by high magnetic field annealing, J. Magn. Magn. Mater. **416**, 61 (2016).

[67] R. Salikhov, L. Reichel, B. Zingsem, R. Abrudan, A. Edström, D. Thonig, J. Rusz, O. Eriksson, L. Schultz, S. Fähler, M. Farle, and U. Wiedwald, Enhanced spin–orbit coupling in tetragonally strained Fe–Co–B films, J. Phys.: Condens. Matter **29**, 275802 (2017).

[68] K. M. Lee, J. W. Choi, J. Sok, and B. C. Min, Temperature dependence of the interfacial magnetic anisotropy in W/CoFeB/MgO, AIP Adv. **7**, 065107 (2017).

[69] L. Chen, S. Mankovsky, S. Wimmer, M. A. Schoen, H. S. Körner, M. Kronseder, D. Schuh, D. Bougeard, H. Ebert, D. Weiss, and C. H. Back, Emergence of anisotropic Gilbert damping in ultrathin Fe layers on GaAs(001), Nat. Phys. **14**, 490 (2018).

[70] A. Stukowski, Visualization and analysis of atomistic simulation data with OVITO-the open visualization tool, Modell. Simul. Mater. Sci. Eng. **18**, 015012 (2009).